

Measurement of the quenching factor of Na recoils in NaI(Tl)

H. Chagani*, P. Majewski, E. J. Daw, V. A. Kudryavtsev & N. J. C. Spooner

Department of Physics and Astronomy, University of Sheffield, Hicks Building, Hounsfield Road, Sheffield S3 7RH, United Kingdom

E-mail: hassan.chagani@ijs.si

ABSTRACT: Measurements of the quenching factor for sodium recoils in a 5 cm diameter NaI(Tl) crystal at room temperature have been made at a dedicated neutron facility at the University of Sheffield. The crystal has been exposed to 2.45 MeV mono-energetic neutrons generated by a Sodern GENIE 16 neutron generator, yielding nuclear recoils of energies between 10 and 100 keVnr. A cylindrical BC501A detector has been used to tag neutrons that scatter off sodium nuclei in the crystal. Cuts on pulse shape and time of flight have been performed on pulses recorded by an Acqiris DC265 digitiser with a 2 ns sampling time. Measured quenching factors of Na nuclei range from 19% to 26% in good agreement with other experiments, and a value of $25.2 \pm 6.4\%$ has been determined for 10 keV sodium recoils. From pulse shape analysis, the mean times of pulses from electron and nuclear recoils have been compared down to 2 keVee. The experimental results are compared to those predicted by Lindhard theory, simulated by the SRIM Monte Carlo code, and a preliminary curve calculated by Prof. Akira Hitachi.

KEYWORDS: Scintillators, scintillation and light emission processes (solid, gas and liquid scintillators); Neutron detectors (cold, thermal, fast neutrons); Gamma detectors (scintillators, CZT, HPG, HgI, etc).

*Corresponding author

Contents

1. Introduction	1
2. Theoretical overview	2
3. Experimental apparatus	5
4. Measurements	9
4.1 Gamma-ray calibration	9
4.2 Event selection by pulse shape discrimination in BC501A	10
4.3 Event selection by time of flight	13
4.4 Event selection by pulse shape discrimination in NaI(Tl)	14
5. Results	16
6. Conclusion	18

1. Introduction

Astronomical observations, such as galactic rotation curves [1] and gravitational lensing [2], combined with measurements of the temperature fluctuations in the Cosmic Microwave Background [3] and abundances of light nuclei [4], point to the striking conclusion that the majority of matter in the Universe does not consist of the stars, planets and gas that are visible in the images from telescopes. A possible solution to this is the presence of a more elusive particle population of ‘Dark Matter’, that contributes to most of the mass of galaxies. Earth-based detectors for dark matter particles passing through the Earth typically utilise large masses of ultra-radiopure target materials, in what is referred to as the direct method. Of the many possible candidates, the Weakly Interacting Massive Particle (WIMP) has the most direct search experiments dedicated to its discovery. Direct searches for WIMPs detect the elastic recoil of an incident WIMP off a target nucleus. Such an interaction deposits a recoil energy E_R in the detector. A variety of approaches to the direct detection of dark matter are adopted by various international collaborations. A recent comprehensive review is given by [5].

Inorganic crystal scintillators are popular choices as target materials for direct dark matter search experiments. The high light yield and pulse shape differences between nuclear and electron recoils explain why thallium activated sodium iodide (NaI(Tl)) crystals are the oldest scintillators used in such experiments [6]. They still remain one of the best detectors at determining spin-dependent WIMP-nucleon limits, and the ANAIS [7], DAMA/NaI [8] and ELEGANT-V [9] direct search experiments utilise them. The DAMA/NaI experiment is the only one that has claimed to

witness the annual modulation of a WIMP signal [8] [10], and until recently, NAIAD [11] held the best spin-dependent limit on WIMP-proton interactions [12]. DAMA/LIBRA [13] is a next generation NaI(Tl)-based detector currently taking data at Gran Sasso. Hence, NaI(Tl) remains an important detector material in non-baryonic dark matter searches.

Energy scale calibration is performed by exposing the detector to radiation from a gamma-ray emitting radioisotope. Unlike neutrons and WIMPs, detectable energy from gamma-rays is a result of collisions with target electrons rather than nuclei. The energy deposited by nuclear recoils is less than that for electron recoils of the same E_R , which is known as ionisation quenching [14] [15]. In other words, $E_{\text{vis}} = QE_R$, where E_{vis} is the visible energy, and Q is the measurable quantity showing the degree of quenching for nuclear recoils with respect to electron interactions, also known as the quenching factor. When calculating the WIMP-nucleon differential cross-section to derive a limit as outlined in [16], this effect can be corrected for by multiplying the detected energy by the reciprocal of the quenching factor. It is necessary to determine the quenching factor for each scintillating dark matter target independently. Additionally, the scintillation efficiency changes depending on the recoil energy, and combined with form factor corrections to the WIMP-nucleon differential cross-section that favour low energy recoils [16], it is important to conduct measurements at energies relevant to dark matter searches (below 50 keV).

Quenching factors of Na recoils in NaI(Tl) have been measured by [17] [18] [19] [20] to a minimum recoil energy of 15 keV. The experiment described here has probed the quenching factor to a lower recoil energy of 10 keV, and has achieved the highest accuracy above 20 keV. Between the energy range 10 to 100 keV, it provides the most detailed measurement of the quenching factor to date.

2. Theoretical overview

After a nuclear interaction, a recoiling nucleus will lose energy as it moves through a target material through collisions with electrons (hereafter called electronic energy loss, resp. electronic energy loss mechanism) and other nuclei. As most detectors, including scintillators, are sensitive to electronic energy loss only, the quenching factor can be calculated through an understanding of these mechanisms. In other words, scintillation light can be understood to be the result of the electronic energy loss mechanisms, while non-radiative transfers, such as heat, are due to collisions with other nuclei. The Lindhard theory [21] [22] attempts to quantify these interactions from first principles, and the points relevant to the theoretical determination of the quenching factor are briefly outlined here.

The energy loss mechanisms through the electronic and nuclear channels can be understood as the electronic and nuclear stopping powers respectively. These can be defined by rescaling the range R and energy E_R of a recoiling nucleus to the respective non-dimensional variables ρ and ε [21]. In such a way, the nuclear energy loss $\left(\frac{d\varepsilon}{d\rho}\right)_n$ can be defined as a universal function $f(\varepsilon)$ that can be calculated numerically.

When the penetrating particle and the atoms of the medium are the same, ε becomes:

$$\varepsilon = \frac{11.5}{Z^3} E_R \quad (2.1)$$

where Z is the atomic number of the target nuclei and E_R is the deposited energy in keV.

The electronic energy loss is defined by $\left(\frac{d\varepsilon}{d\rho}\right)_e = \kappa\sqrt{\varepsilon}$. If the penetrating particle is identical to the atoms of the medium, the constant κ is given by:

$$\kappa = \frac{0.133Z^{\frac{1}{2}}}{\sqrt{A}}\xi_e \quad (2.2)$$

where A is the mass number of the target nuclei and $\xi_e \approx Z^{\frac{1}{2}}$ from [21].

Assuming that the electronic and nuclear collisions are uncorrelated, the total energy given to electrons and that given to atoms can be expressed as the two separate quantities η and $\bar{\nu}$ respectively. The non-dimensional variable ε can now be written in terms of these:

$$\varepsilon = \bar{\eta} + \bar{\nu} \quad (2.3)$$

For large ε , the mean energy given to atoms of the medium $\bar{\nu}$ is inversely proportional to κ . However, this does not hold when $\varepsilon < 1$, in which case $\bar{\nu} \approx \varepsilon$. A single formula that combines these results is [22]:

$$\bar{\nu} = \frac{\varepsilon}{1 + \kappa g(\varepsilon)} \quad (2.4)$$

where the function $g(\varepsilon)$ is well fitted by [16]:

$$g(\varepsilon) = 3\varepsilon^{0.15} + 0.7\varepsilon^{0.6} + \varepsilon \quad (2.5)$$

From Eq. (2.3), the mean energy given to electrons $\bar{\eta}$ in terms of ε can be written as $\bar{\eta} = \varepsilon - \bar{\nu}$. Therefore, an expression for the quenching factor can be obtained using its definition as given previously, by dividing $\bar{\eta}$ by ε through a combination of Eq. (2.3) and Eq. (2.4):

$$\frac{\bar{\eta}}{\varepsilon} = \frac{\varepsilon - \bar{\nu}}{\varepsilon} = \frac{\varepsilon(1 + \kappa g(\varepsilon)) - \varepsilon}{\varepsilon(1 + \kappa g(\varepsilon))} = \frac{\kappa g(\varepsilon)}{1 + \kappa g(\varepsilon)} \quad (2.6)$$

By substituting Eq. (2.1), Eq. (2.2) and Eq. (2.5) into Eq. (2.6), the quenching factor can be expressed as a function of nuclear recoil energy. The theoretical dependence of the quenching factor for sodium recoils in $^{23}_{11}\text{Na}$ is shown in Figure 1. As $^{23}_{11}\text{Na}$ and $^{127}_{53}\text{I}$ have significantly different mass and atomic numbers, the quenching factor of sodium recoils in sodium, and those in iodine are not similar. In the case of sodium recoils in iodine, the evaluation of the quenching factor is more complicated, and Eq. (2.6) can no longer be used. Lindhard theory can only approximate the quenching factor in such cases at very low energies [22].

A key requirement of the Lindhard theory is that electronic and nuclear collisions can be separated. However, the repulsion between two interacting nuclei makes part of the parameter range unavailable for transferring energy to electrons. As a result, the electronic stopping power is suppressed when $\varepsilon \ll 1$, leading to the non-proportionality of $\left(\frac{d\varepsilon}{d\rho}\right)_e$ with $\sqrt{\varepsilon}$ in this energy range [23]. This can be corrected for by replacing ξ_e in Eq. (2.2) with the function $\tau\left(\varepsilon, \frac{Z_1}{Z_2}\right)$ given in [23], where Z_1 and Z_2 are the atomic numbers of the penetrating and target nuclei respectively. The impact of this correction on light nuclei, such as sodium, is very small, and as such it is not evaluated here.

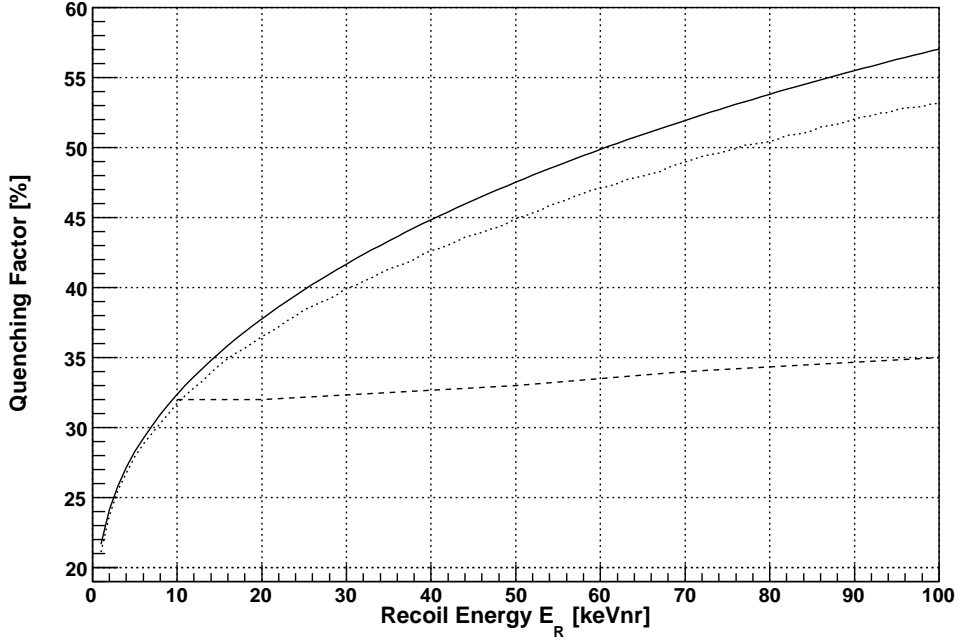


Figure 1. Theoretical curves for the quenching factor of sodium recoils. The solid black curve represents the quenching factor of sodium recoils in sodium derived from Lindhard theory [21] [22]. The preliminary curve of the quenching factor of sodium recoils in NaI(Tl) from [25] is illustrated by the dashed line. Finally, the result derived from TRIM [28] for Na recoils in NaI(Tl) is shown by the dotted line.

In semiconductors, the measured quenching factor agrees well with that given by Eq. (2.6). For scintillators, however, some degree of quenching also affects the electronic energy loss by ions (energy loss due to excitation and ionisation) [24] for high Linear Energy Transfer (LET). The absolute quenching factor for nuclear recoils q_n given by Eq. (2.6) is not the required correction factor to the differential WIMP-nucleon event rate. The quenching factor of nuclear recoils relative to those from electron interactions Q can be approximated by [24]:

$$Q = \frac{q_n q_e}{S_\gamma} \quad (2.7)$$

where q_e is the electronic quenching factor (quenching factor for electronic energy loss of ions) and S_γ is the scintillation efficiency for electron recoils. If the quenching factor for sodium recoils in Na from Eq. (2.6) is defined as q_n in Eq. (2.7), then an overestimation for the quenching factor of sodium recoils in NaI(Tl) will result [25].

The response of NaI(Tl) to photons is known to be non-linear [26] [27] with energy. Therefore, the choice of gamma source for detector calibration plays some role in the final quenching factor, as a linear energy distribution is assumed in dark matter experiments. Using the response curve from [26], S_γ is equal to 0.9 for 122 keV gamma-rays. The preliminary theoretical curve of the quenching factor of Na recoils in NaI(Tl) from [25] is shown in Figure 1.

The Stopping and Range of Ions in Matter (SRIM) package [28] simulates the process of ions impinging onto various target materials. The program calculates the stopping power and range of ions in matter using a quantum mechanical treatment of ion-atom collisions. These parameters are used by the TRansport of Ions in Matter (TRIM) program [28] to calculate the final distribution of the ions. All the energy loss mechanisms associated with ion-atom collisions, such as target damage, sputtering, ionisation and phonon production, are also evaluated. The quenching factors for various materials have been simulated with these programs [29], and that for sodium recoils in NaI(Tl) is determined here using the same technique.

A NaI(Tl) crystal of density 3.67 g/cm^3 is defined as the solid target. Sodium ions are given an initial energy (in other words, a recoil energy) and propagated through the crystal at a normal incidence angle. Recoil energies are varied between 1 and 100 keV, in 1 keV steps, and 4 000 ions are simulated at each energy.

The percentage energy loss from the original ions and the resultant recoiling atoms induced by ion-atom collisions is calculated by TRIM. This is then subdivided into energy losses from ionisation, vacancies from un-filled holes left behind after a recoil atom moves from its original site, and phonon emission. Light emission is a result of ionisation, and hence, the sum of the percentage energy loss due to ionisation from the original ion and recoiling atoms is the quenching factor. The mean of these contributions over 4 000 events is evaluated by TRIM, and the results are shown in Figure 1.

Unlike the prediction of the quenching factor from [25], the result from TRIM follows the shape of the Lindhard curve. However, although they display similar values at low energies, the quenching factor from Lindhard theory rises faster with increasing energy. At 10 keVnr, all three results are in good agreement, and it is after this point that they start to diverge. The most comprehensive treatment to the evaluation of the quenching factor is that given by [25] (Eq. (2.7)). Therefore, it is reasonable to assume that the measurements of Q will more closely match the shape of this curve, although their values should lie below it.

The quenching factor can be measured by inducing nuclear recoils of a known energy in the target material. In this way, the ratio of measured energy through electronic energy losses to known recoil energy can be determined. In the case of NaI(Tl), iodine recoils will also occur. However, it is clear from Eq. (2.6) that the degree of quenching for heavy nuclei such as iodine is significantly greater than that for lighter nuclei such as sodium. This means that a low energy threshold is required to witness iodine recoils. As the purpose of this paper is the measurement of Na recoil in NaI(Tl), such a threshold is not attained, and hence iodine recoils will not be visible.

3. Experimental apparatus

Two Sodern GENIE 16 neutron generators are housed within a dedicated neutron laboratory at the University of Sheffield. The deuterium-deuterium and deuterium-tritium accelerators produce an isotropic distribution of 2.45 MeV and 14.0 MeV mono-energetic neutrons respectively. All electronics and data acquisition equipment are located in the control room, which is isolated from the experimental hall by 3 ft of concrete shielding. During operation, the beam is placed into a concrete castle to provide additional shielding.

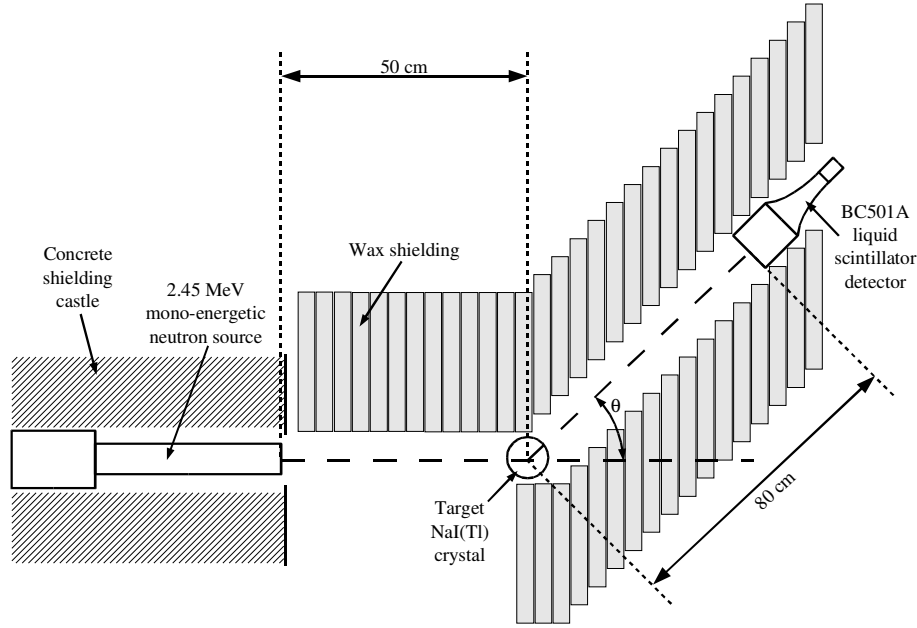


Figure 2. Schematic view of the detector arrangement used to measure scintillation from nuclear recoils in NaI(Tl).

A schematic view of the detector arrangement is shown in Figure 2. Only the deuterium-deuterium neutron beam is used for these measurements. Neutrons of energy 2.45 MeV pass through a hole in the concrete castle. They travel 50 cm before reaching the centre of the NaI(Tl) crystal. The energy deposited E_R as a function of the scattering angle is given by:

$$E_R \approx \frac{2m_A E_n m_n}{(m_A + m_n)^2} \cdot (1 - \cos \theta) \quad (3.1)$$

where m_A is the mass of the target nucleus, E_n is the energy of incident neutrons, m_n is the mass of the neutron and θ is the scattering angle. Scattered neutrons are detected by a secondary BC501A liquid scintillator detector, which is placed at an angle θ for the recoil energies of interest E_R .

NaI(Tl) crystals are hygroscopic and need to be encased within an air-tight container. The 5 cm diameter, 5.4 cm long, cylindrical NaI(Tl) crystal used here is encased within a hollow aluminium cylinder of wall thickness 2.5 mm. A glass window, of thickness 2.5 mm and diameter 5 cm, is optically coupled to the crystal with silicon oil to improve light collection. The reflection of light off the inner walls is increased by the wrapping of 1 mm thick PTFE tape around the crystal. A 3-inch ETL 9265KB photomultiplier tube (PMT) [30] is optically coupled to the glass window. As the energy of the calibration source is significantly higher than the nuclear recoil energies in this experiment, a tapered voltage divider network is chosen and constructed for the PMT. Such a system reduces space charge effects, which lead to a non-linear response where high-energy pulses appear smaller than they actually are.

The secondary detector consists of a cylindrical aluminium vessel of diameter 7.8 cm and height 8.0 cm filled with BC501A liquid scintillator. The active volume is viewed by an ETL 9288B PMT [30] at an operating voltage of -1300 V.

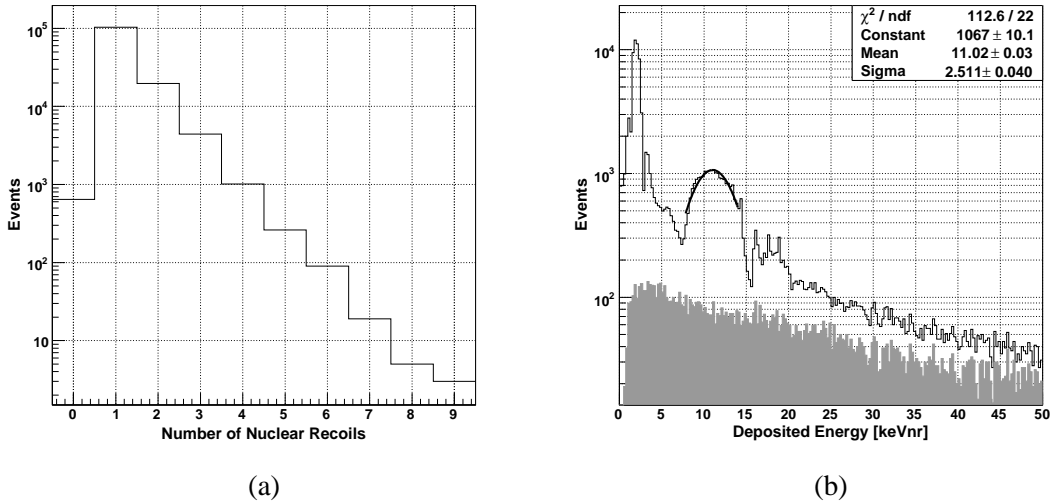


Figure 3. Simulated distributions of: (a) number of nuclear recoils in NaI per neutron; and (b) total energy deposited in NaI(Tl) crystal. A significant proportion of events do result in multiple scattering, as shown in (a). However, the deposited energy spectrum for events as a result of two or more nuclear recoils, represented by the shaded area in (b), is featureless. This implies that their contribution to the background should not interfere with the signal peak position at approximately 10 keVnr. The peak at approximately 2 keVnr in (b) is from iodine recoils, which is not visible in real data at this scattering angle due to the higher energy threshold. Features either side of the recoil peaks in (b) are due to neutrons scattering off nuclei within the wax shielding before entering the secondary detector, and those that escape through gaps between the BC501A cylinder and wax walls. The contribution to background from these interactions at other deposited energies is featureless.

Only events with a single interaction in the crystal contribute to the recoil energy E_R at a given scattering angle θ in Eq. (3.1). Multiple interactions lead to neutrons depositing a range of possible energies in the crystal before being detected by the secondary BC501A detector, thus contributing to the background. Due to the cylindrical geometry of the crystal, a Monte Carlo simulation is required to obtain an accurate probability for multiple interactions.

The geometry of the experiment, illustrated in Figure 2 is replicated within the GEANT4 framework [31], where 2.45 MeV neutrons are generated at the face of the neutron source and fired towards the NaI(Tl) crystal. A total of 10^8 events are generated at scattering angles associated with 10 and 100 keVnr sodium recoil energies as given by Eq. (3.1). Only events that deposit energy in both the crystal and BC501A detector are recorded. Approximately 0.13% of 10 keVnr and 0.05% of 100 keVnr events satisfy this condition. The reason for this asymmetry is the non-isotropic cross-section for neutron scattering at higher recoil energies and for heavier nuclei [32].

Simulation results at 10 keVnr nuclear recoil energy are shown in Figure 3. Although a significant proportion of events undergo multiple scattering in the crystal, the deposited energy from these interactions, represented by the shaded histogram, is featureless in comparison with the total recoil energy spectrum. Therefore, there is no preferential energy deposition, and the number of multiple interactions should make no difference to the final result.

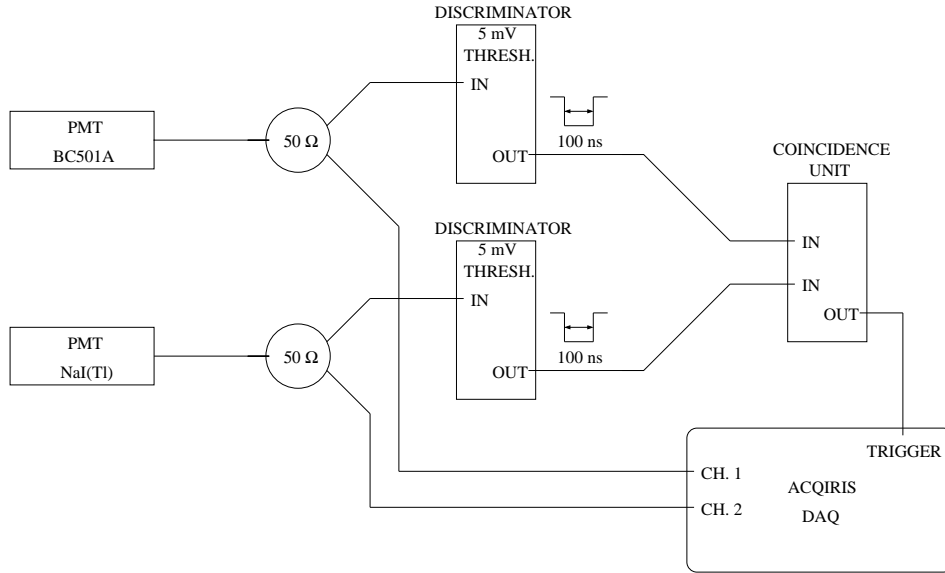


Figure 4. Hardware trigger electronics for the quenching factor experiment. Analogue photomultiplier signals from the BC501A detector and NaI(Tl) crystal are split with a $50\ \Omega$ power divider, and sent to a discriminator and an input channel on the DAQ. The discriminator is set at a threshold of 5 mV, and a 100 ns wide NIM pulse is sent to a 2-fold coincidence unit. If the signals are coincident, a NIM pulse provides the external trigger to the DAQ.

The inclusion of nuclear recoils off iodine nuclei also results in a low energy peak at approximately 2 keV_{nr} from single scattered neutrons as shown in Figure 3(b). From Eq. (3.1), the change in energy with scattering angle is far more pronounced for lighter nuclei, and as iodine has a significantly higher mass number than sodium, such a result is expected. For the reasons outlined in Section 2, such a peak would not be visible in the measured data, and will not interfere with the sodium peak.

The configuration of electronics for the hardware trigger is shown in Figure 4. Analogue photomultiplier signals from the NaI(Tl) crystal and BC501A detector are split with a $50\ \Omega$ power divider. The signal from each PMT is then sent simultaneously to a discriminator set at a threshold of 5 mV, and a channel of the data acquisition system (DAQ). The hardware trigger is two signals coincident within a 100 ns time window. The analogue pulses are converted to digitised waveforms by an 8-bit, 2-channel Acqiris digitiser [33] with a 500 MHz sampling rate. Data acquisition software running on a linux computer, similar to that used by the ZEPLIN-II experiment [34], reads out the digitised waveforms and writes them to disk.

An analysis program reads the binary data output of the digitiser. The program goes through each event, extracting the amplitude at each 2 ns sampling point and placing the values into an array. To assign a baseline, the mean and standard deviation of the first 200 ns of a waveform are determined. This process is then repeated over the same time window, excluding bins of amplitude greater than three standard deviations from the mean. The baseline is calculated in this manner on an event-by-event basis, and this procedure results in an improvement to its estimation.

An event viewer is implemented within the ROOT framework [35]. Waveform parameters are

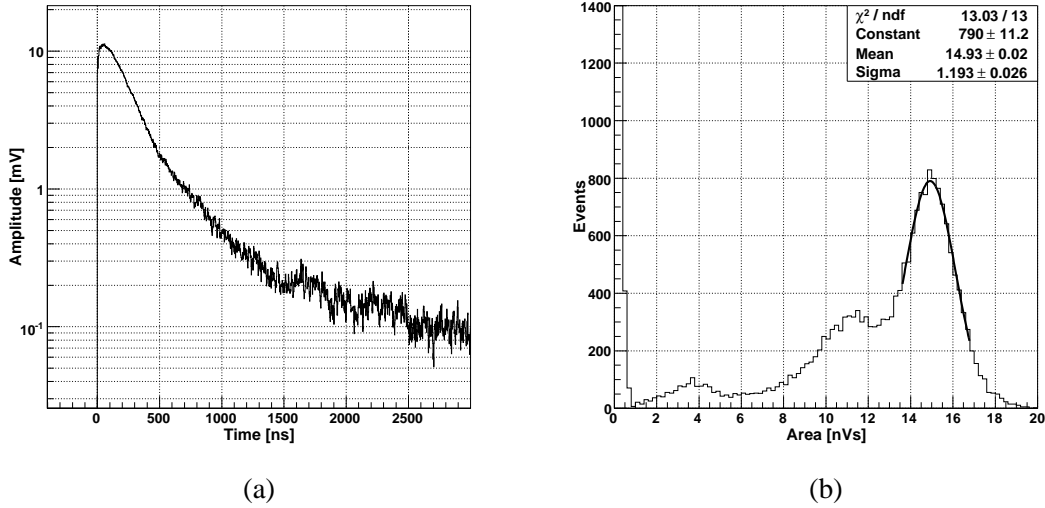


Figure 5. (a) Pulse shape for an event induced by 30 keV X-rays from ^{129}I source. Pulses that contribute to the 30 keV peak are extracted and their amplitudes are summed. The pulse is normalised to 1 event. (b) Calibration of NaI(Tl) crystal detector with 122 keV gamma line from ^{57}Co . Three clear peaks are visible corresponding to X-rays, X-ray escape peak and total absorption at approximately 3.5, 11.5 and 15 nVs respectively.

extracted and stored in a ROOT tree for later analysis. The total pulse area, which is proportional to the deposited energy, is the sum of digitised bin contents within a range:

$$\sum_{i=s_1}^{s_2} V_i(t)\Delta t = \int_{t_1}^{t_2} V(t)dt \quad (3.2)$$

where s_1 is the first and s_2 the second sampling point over which the summation is performed. The value of s_1 is the first point at which the pulse reaches 10% of its maximum amplitude. The amplitude of each bin i is denoted by $V_i(t)$, and with a 500 MHz sampling rate, $\Delta t = 2$ ns. The start t_1 and stop t_2 times are defined as $t_{1,2} = s_{1,2}\Delta t$.

4. Measurements

4.1 Gamma-ray calibration

A constant value for t_2 in Eq. (3.2) needs to be defined to obtain the area under NaI(Tl) pulses. It is difficult to determine t_2 from a single pulse, due to the sparse distribution of photons in the tail region. Instead, a scintillation pulse is built from the sum of 10 000 pulses detected when the crystal is irradiated by 30 keV X-rays from ^{129}I source, as shown in Figure 5. The amplitudes are normalised to reproduce the mean shape of one pulse.

Photons from scintillation light continue well beyond 3 μs . However, electronic noise in the tail region makes it difficult to choose a relatively large value for t_2 . A compromise of 2 μs after the start of the pulse is used, which is equivalent to about 92% of the total waveform.

The crystal is exposed to gamma-rays from a variety of radioactive sources, between 30 keV (X-rays from ^{129}I) and 662 keV (^{137}Cs γ -rays). A decrease in photon response is observed at the iodine K-shell absorption edge at 33.2 keV, consistent with other studies [26] [27]. Therefore, determination of the energy scale must be performed in a region where a linear response is observed. Calibration is performed with the 122 keV gamma line from a ^{57}Co source to establish an electron equivalent energy scale (labelled keVee as opposed to keVnr for nuclear recoil energies), as shown in Figure 5. A light yield of 5.1 photoelectrons/keV is found. The procedure is repeated approximately every 3 hours to analyse any drift in the light yield, and if significant degradation is witnessed the crystal is recoupled to the PMT.

An attenuation coefficient of around $1.01 \text{ cm}^2/\text{g}$ for 122 keV ^{57}Co gamma-rays traversing NaI(Tl) translates to a mean free path length of 2.7 mm. Therefore, most interactions will occur near the surface of the crystal, and hence may be affected by defects. To check for deformities, the light yield at 30° angles around the crystal is checked. All but one point lie within one standard deviation of the mean light yield. Therefore, the use of ^{57}Co for calibration is acceptable, as no major surface defects are present.

A suitable full scale (range) over which to digitise the signal needs to be chosen. Using the Lindhard curve for sodium recoils in Na from Figure 1, a 50 keV nuclear recoil will be quenched by 48%, resulting in a 25 keV electron equivalent pulse. This is equivalent to a pulse close to that from a 30 keV X-rays from ^{129}I . With an amplitude of just over 11 mV, a range of 50 mV is adequate for this experiment.

Low level cuts include removing pulses that saturate the digitiser and are not in coincidence. The latter are caused when the DAQ triggers on the end of an event.

4.2 Event selection by pulse shape discrimination in BC501A

A secondary detector is required to identify neutrons that scatter off the target nuclei at the nuclear recoil energies given by Eq. (3.1). As the main background is from gamma-rays, a detector material with a high discrimination power is a major requirement. Enhanced emission of the slow component and a high hydrogen-to-carbon ratio make the BICRON Corporation BC501A organic liquid scintillator ($\text{C}_6\text{H}_4(\text{CH}_4)_2$), equivalent to Nuclear Enterprises NE213, well-suited for this purpose.

As with the NaI(Tl) pulses described previously, a suitable value for t_2 in Eq. (3.2) needs to be determined. From the typical 600 keVee pulses in Figure 6, a value of 100 ns after the position of the maximum bin is defined as the end of the waveform.

The intensity of these pulses $I(t)$ can be written to good approximation as a function of four exponentials [36]:

$$I(t) \approx A \left(e^{-\frac{(t-t_0)}{\tau_e}} - e^{-\frac{(t-t_0)}{\tau_1}} + \frac{B}{A} e^{-\frac{(t-t_0)}{\tau_e}} - \frac{B}{A} e^{-\frac{(t-t_0)}{\tau_2}} \right) \quad (4.1)$$

where τ_e is the RC time constant of the data acquisition electronics, τ_1 and τ_2 are the decay time constants of the fast and slow components respectively, and A and B are their respective intensities. Due to the loose definition of the pulse start time, an additional parameter for time reference t_0 is defined.

The ratio $\left| \frac{B}{A} \right|$ in Eq. (4.1) provides a measure of the discrimination power, making use of the characteristic enhanced emission of the slow component in BC501A [36]. The fitting of each pulse

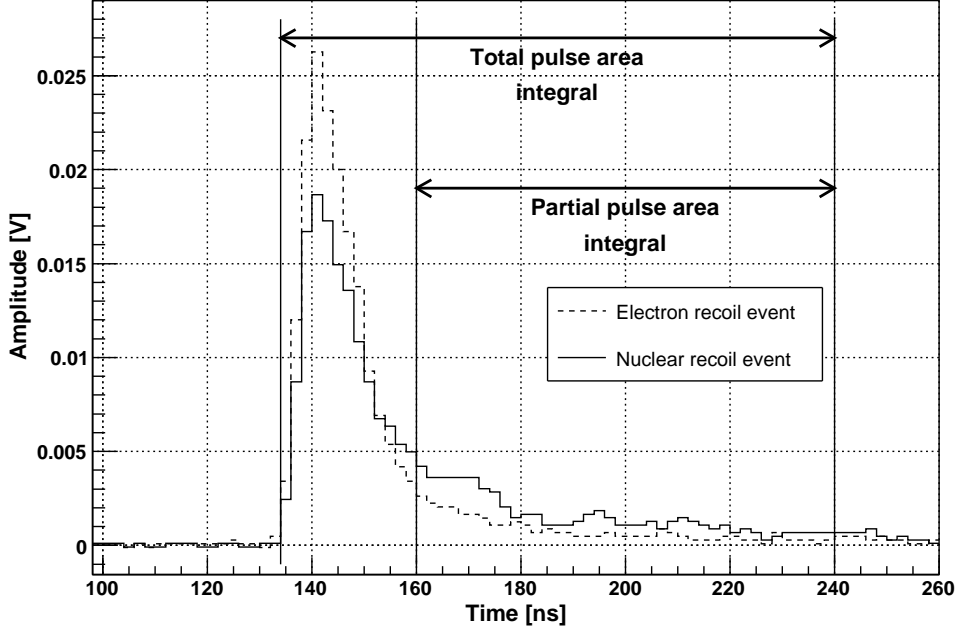


Figure 6. Typical pulses from 600 keV nuclear and electron recoils in the BC501A detector. Energy scale calibration is performed with the 662 keV gamma line from a ^{137}Cs source. The total pulse area A is the sum of the bins that lie between the start time and 100 ns after the maximum peak position. The partial pulse area P is the sum of those that lie between 20 ns after the peak position and the end of the waveform.

is a time consuming procedure due to the six free parameters in Eq. (4.1). The time taken for a fit to successfully converge can be improved by restricting parameters, or deriving average values for some and fixing them [36]. However, if the discriminating factor is the ratio of the intensities of the slow to fast components, the same should hold true for the ratio of the slow component to the total intensity of the pulse as $B \ll A$.

Therefore, by integrating over the tail of a pulse and dividing by the total area, neutron and gamma events are separated. The ratio of partial pulse area in the tail P_{nr} to total pulse area A_{nr} will be closer to unity when compared with electron recoils of the same energy $\frac{P_{er}}{A_{er}}$. This can be inferred from [36], where the $|\frac{B}{A}|$ ratio is smaller for electron recoils. In other words:

$$\frac{P_{nr}}{A_{nr}} > \frac{P_{er}}{A_{er}} \quad (4.2)$$

The discrimination technique defined in Eq. (4.2) is tested by exposing the BC501A detector to 662 keV gamma-rays from a ^{137}Cs source and 2.45 MeV neutrons from the deuterium-deuterium beam. The hardware trigger is identical to that shown in Figure 4, with the exception of the NIM pulse from the discriminator acting as the external trigger to the digitiser. Offline saturation cuts are performed on the recorded data.

The results are shown in Figure 7. A lower limit for the partial pulse area integral of 30 ns after the maximum peak position is chosen. The presence of an upper horizontal band of neutrons is seen

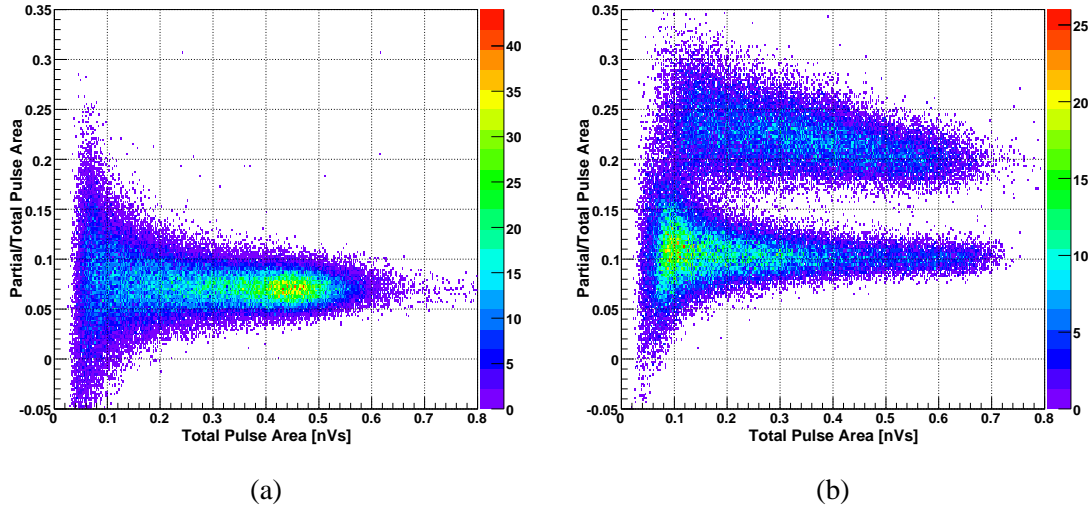


Figure 7. Scatter plots of partial-to-total pulse area ratio against total pulse area in the BC501A detector for: (a) gamma-rays from a ^{137}Cs source; and (b) neutrons from the 2.45 MeV deuterium-deuterium neutron beam and background gamma-rays. The 662 keV gamma line is visible in (a) at approximately 0.45 nVs total pulse area. An upper band of neutron energies is evident in (b). Lower limit of 30 ns after the maximum peak position is implemented for the partial pulse area integrals.

in the data from the neutron run. This band is absent from the gamma-ray data. A large gamma background is apparent in data from the 2.45 MeV deuterium-deuterium beam, emphasising the need for good neutron-gamma discrimination.

By changing the pulse partial area integration boundaries, it may be possible to increase the resolution between neutron and gamma events, and hence decrease the energy threshold for discrimination. The start of the tail is varied between 10 and 50 ns after the maximum peak position, in stages of 10 ns. One dimensional histograms of the partial-to-total pulse area ratio result in two peaks. By fitting Gaussian functions to these peaks, a figure of merit M is used to quantify the neutron-gamma discrimination power:

$$M = \frac{(\bar{x}_n - \bar{x}_\gamma)}{(\sigma_n + \sigma_\gamma)} \quad (4.3)$$

where \bar{x}_n and \bar{x}_γ are the mean positions of the neutron and gamma peaks respectively. The full width half maximum of the neutron and gamma peaks are given by σ_n and σ_γ respectively. Applying Eq. (4.3), M -factors are calculated as shown in Table 1. A lower limit on partial pulse area integral of 20 ns after the position of the peak provides the best resolution power.

Scintillation light from nuclear recoils is quenched in all materials. BC501A is not an exception, and the quenching factor has been found to be non-linear [37]. An electron equivalent scale is established by calibrating the BC501A detector with the 662 keV gamma line from ^{137}Cs . Cutting at total pulse areas greater than 16 nVs, as shown in Figure 8, yields a minimum energy threshold of 280 keVee. Using the non-linear function for the proton quenching factor given by [37], this corresponds to a proton recoil energy of 910 keVnr. Reducing the threshold further does not affect

Lower limit of integration [ns]		Electron recoil peak	Nuclear recoil peak	M
10	\bar{x}	0.2990 ± 0.0002	0.4518 ± 0.0003	2.15 ± 0.02
	σ	0.0324 ± 0.0003	0.0386 ± 0.0005	
20	\bar{x}	0.1555 ± 0.0001	0.2961 ± 0.0003	2.97 ± 0.03
	σ	0.0189 ± 0.0002	0.0284 ± 0.0004	
30	\bar{x}	0.1030 ± 0.0001	0.2155 ± 0.0003	2.90 ± 0.03
	σ	0.0149 ± 0.0002	0.0239 ± 0.0003	
40	\bar{x}	0.0715 ± 0.0001	0.1596 ± 0.0002	2.70 ± 0.03
	σ	0.0125 ± 0.0002	0.0201 ± 0.0003	
50	\bar{x}	0.0482 ± 0.0001	0.1161 ± 0.0002	2.49 ± 0.04
	σ	0.0108 ± 0.0001	0.0165 ± 0.0004	

Table 1. Effects of different lower limits for partial pulse integration (column 1) on the peak positions for BC501A pulses (columns 2 and 3) and figure of merit as defined by Eq. 4.3 (column 4).

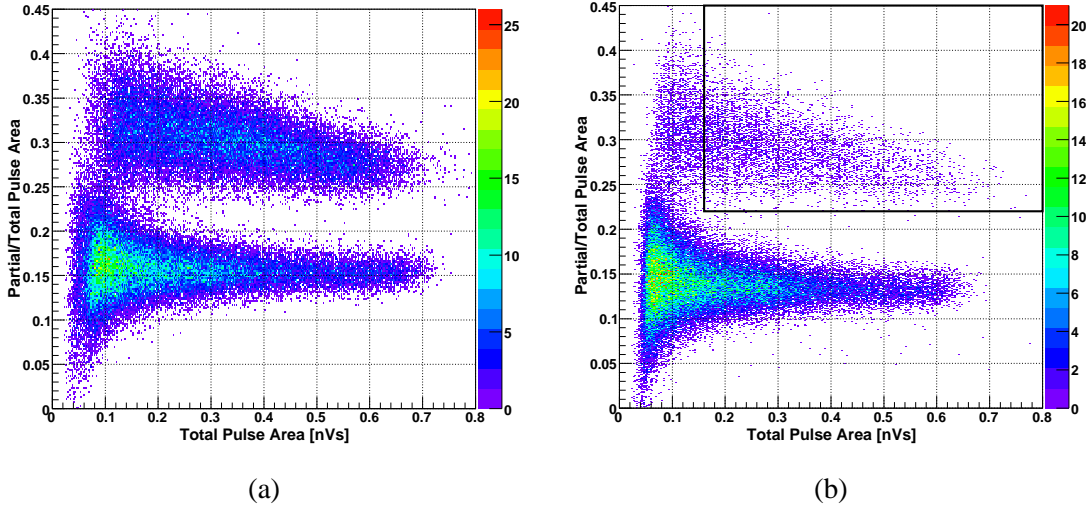


Figure 8. Implementation of pulse shape discrimination cut in the BC501A detector for neutrons from the 2.45 MeV deuterium-deuterium neutron beam. The best separation between gammas and neutrons occurs when the lower limit for partial pulse integral is set to 20 ns after the maximum peak position, as shown in (a). The implementation of this cut is shown for the data taken at 10 keVnr in (b), where events that lie within the black box are accepted. A minimum energy threshold of 280 keVee is attained.

the resulting quenching factor.

4.3 Event selection by time of flight

As the rest mass energy of incident neutrons is far greater than their kinetic energy of 2.45 MeV, they are non-relativistic. With reference to Figure 2, after interacting with the crystal, the non-

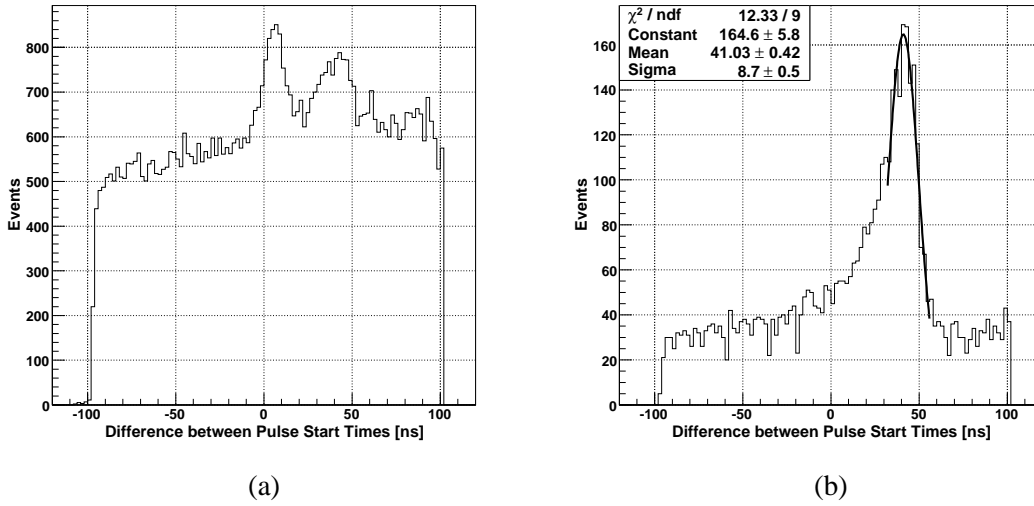


Figure 9. Time of flight distributions between NaI(Tl) crystal and BC501A detector for data taken at 10 keVnr: (a) before; and (b) after performing the cut on pulse shape discrimination in BC501A. Gamma and neutron peaks at approximately 0 and 40 ns are visible in (a). After the cut on pulse shape is implemented, it becomes possible to fit a Gaussian function to the neutron peak in (b).

relativistic neutrons will take longer to reach the secondary BC501A detector than gamma-rays. This time of flight t can be quantified with:

$$t [\text{ns}] \approx 3.336 \cdot s [\text{m}] \sqrt{\frac{m_n [\text{MeV}]}{2E_n [\text{MeV}]}} \quad (4.4)$$

where s is the distance travelled by the neutron. As $E_R \ll E_n$, the recoil energy is ignored to good approximation in Eq. (4.4). For $E_n = 2.45$ MeV, Eq. (4.4) yields a value of 38 ns for the time of flight.

In Figure 9, prior to the cut on BC501A pulse shapes outlined previously, two peaks are visible at approximately 0 and 40 ns corresponding to gamma-rays and neutrons, respectively. The time of flight differs from that expected due to a time delay in the cables and the possibility of a neutron to interact anywhere along the 8 cm depth of liquid scintillator that it traverses. From Figure 2, $s = 80$ cm is the distance from the centre of the crystal to the face of the secondary detector. Substituting a value of $s = 88$ cm into Eq. (4.4) results in an upper limit of 42 ns. This is confirmed from the simulated time of flight distributions for scattering angles associated with 10 and 100 keVnr energy depositions in Figure 10. A sharp decline is witnessed in the number of events that contribute to the simulated neutron peaks after 42 ns.

Due to the large background from gamma-rays, it is difficult to fit a Gaussian function to the measured neutron peak in Figure 9a. However, after cutting on neutron events in the BC501A detector, as shown in Figure 9b, the neutron peak becomes clearly visible.

4.4 Event selection by pulse shape discrimination in NaI(Tl)

A variety of pulse shape discrimination techniques can be employed to discriminate low energy

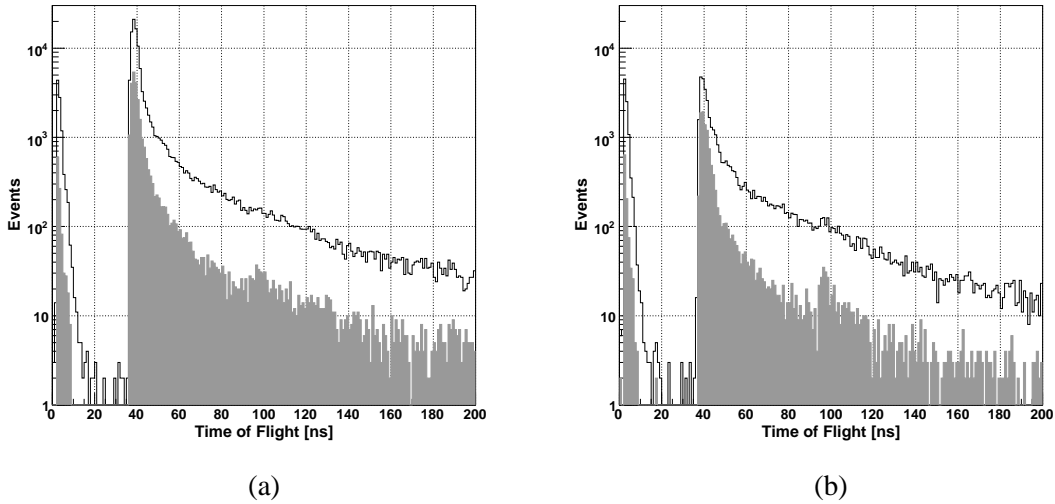


Figure 10. Simulated time of flight distributions between NaI(Tl) and BC501A detector for scattering angles associated with: (a) 10 keVnr; and (b) 100 keVnr energy depositions. The unshaded histogram includes all events, while the shaded one only consists of single scattered events in the crystal. The peaks at 0 ns are from gamma-rays produced by inelastic scattering in the crystal. A decrease in events is seen at higher times. The delayed events are due to the scattering of neutrons off the wax shielding.

nuclear and electron recoils in inorganic crystal scintillators. Discrimination using mean time, neural networks and log likelihood have been investigated in CsI(Tl) crystals [38]. No significant difference in efficiencies between the techniques was observed at energy scales relevant to dark matter searches.

The scintillation mechanism of CsI(Tl) is similar to that of NaI(Tl), so there is no reason to believe that the same result would not be true here. Therefore, mean time is used for nuclear-electron recoil discrimination as it is the easiest to implement with digitised waveforms. The reduction code calculates the mean time $\langle t \rangle$ for each event with:

$$\langle t \rangle = \frac{\sum_{i=s_1}^{s_2} A_i t_i}{\sum_{i=s_1}^{s_2} A_i} \quad (4.5)$$

where A_i is the amplitude of the digitised pulse and t_i is the time relative to the start of the pulse at sampling point i .

The vast majority of gamma events have been rejected by performing the lower level cuts on PSD in BC501A and time of flight, as outlined above. Additional improvement is achieved by plotting mean time distributions of events and removing those which lie more than a half of a standard deviation from the peak position of the Gaussian fit (see Figure 11a). This is illustrated by the clear peak present in the resultant electron equivalent energy distribution for 10 keVnr Na recoils in Figure 11b.

To assess the discrimination power of NaI(Tl), mean time distributions from gamma-rays are compared with those from neutrons. The 511 keV gamma-ray from a ^{22}Na source has a number of properties that make it attractive for such a measurement. Neutrons will interact throughout

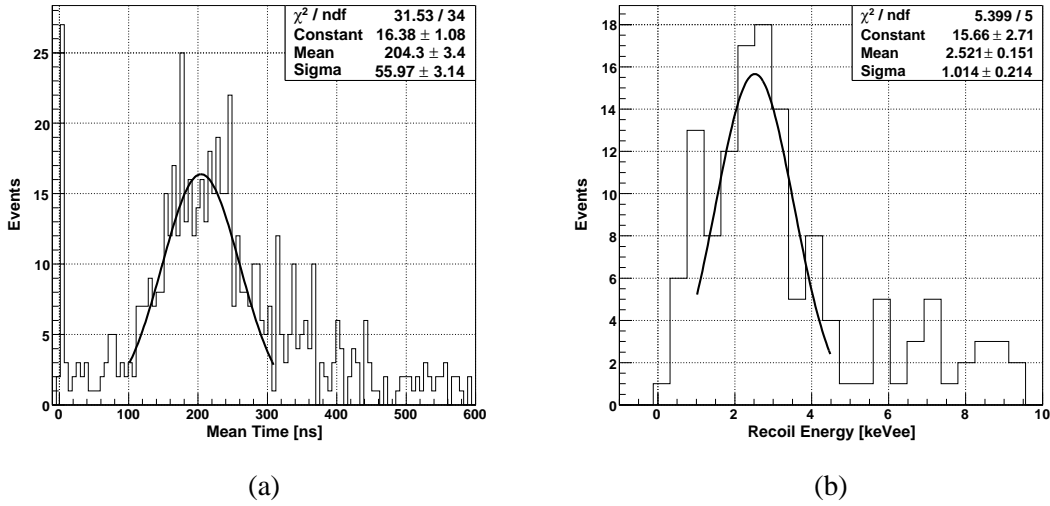


Figure 11. (a) Mean time of pulses from 10 keVnr Na recoils. (b) Recoil energy in electron equivalent scale after events that lie more than half a standard deviation from the mean in (a) are excluded. The result in (b) indicates the quenching factor for 10 keVnr Na recoils in NaI(Tl) is 25.21%.

the bulk of the crystal, and gamma-rays of this energy have a typical penetration depth of 29 mm. Additionally, the interaction cross-section in NaI(Tl) is dominated by Compton scattering at this energy, meaning that a significant number of gamma-rays will deposit a fraction of their energy in the crystal before escaping. Finally, their back-to-back emission is exploited by placing the source between the crystal and BC501A detector, and operating them in coincidence using the electronics shown in Figure 4. The width of NIM pulses from the discriminator is reduced to 10 ns, which is the minimum setting, as coincident gammas will arrive at each detector at the same time. This enables the discriminator threshold to be decreased to 2 mV without noisy events polluting the data.

Mean time values for electron recoils are evaluated in 2 keVee wide energy bins, each containing approximately 6 000 events. Values for nuclear recoils come from the data taken with the neutron beam at each scattering angle (see Table 2). The results, from Figure 12, indicate that mean time values for sodium recoils stay roughly constant with energy (only small increase is seen above 15 keV), compared with those from Compton scatters (electron recoils) that increase significantly, in agreement with [18] [19]. Additionally, it becomes difficult to distinguish electron and nuclear recoils at energies below 4 keVee, hampering the sensitivity of NaI(Tl) dark matter detectors.

5. Results

Distributions similar to that shown in Figure 11b are constructed for different energy bins in keVnr scale. The areas around the peaks are fitted to the Gaussian function, the peak positions of the fits being associated with the measured (or electron equivalent) energy. The quenching factors for each energy bin are determined as the ratio of electron equivalent to recoil energy. Values of the measured energies and resultant quenching factors at each scattering angle are given in Table 2.

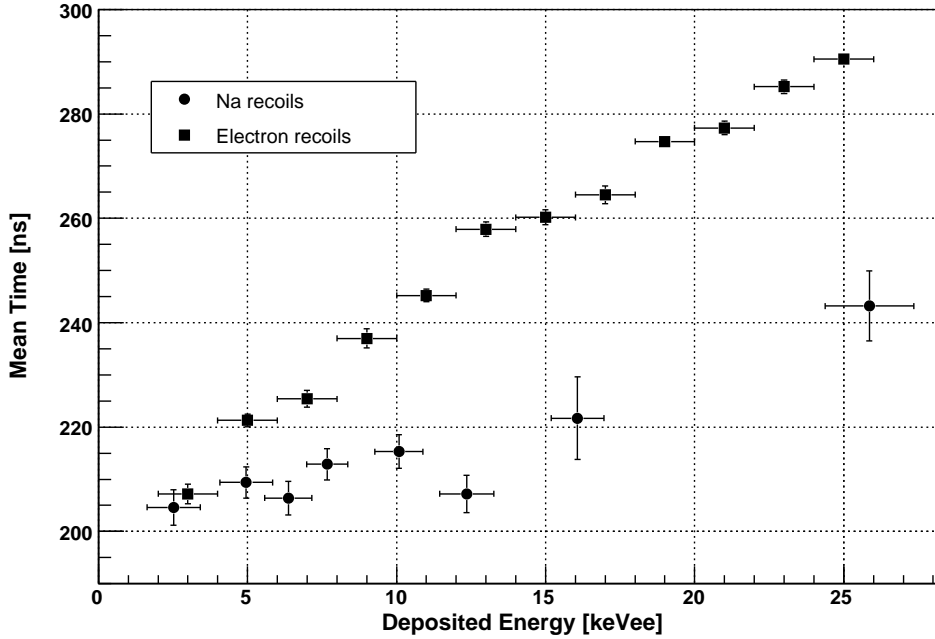


Figure 12. Mean time as a function of deposited energy for sodium (Na) and electron recoils. Measurements of Na recoils are performed with the neutron beam. Compton electrons are induced by gamma-rays from a ^{22}Na source.

The quenching factor of sodium recoils in NaI(Tl) varies between 19% and 26% in the range 10 to 100 keVnr, in agreement with previous experimental results [17] [18] [19] [20], as shown in Figure 13. A scintillation efficiency of $25.2 \pm 6.4\%$ has been determined for 10 keVnr Na recoils.

Systematic errors in the measurement of the scattering angle start to dominate at energies less than 20 keVnr. Although it may be possible to take a measurement at 5 keVnr, especially as the light yield seems to increase at lower nuclear recoil energies, the magnitude of the systematic error at such a scattering angle would be too large to obtain a sensible result. Therefore, the limiting factor in this experiment is not the light yield, but the error associated with the scattering angle.

There are a number of features in Figure 13, including a dip in the quenching factor around a nuclear recoil energy of 40 keVnr, and subsequent rise at lower energies. This is the first time a dip has been observed. The measurement performed here is the most comprehensive study of the quenching factor of sodium recoils in NaI(Tl) to date in the low energy regime. It is therefore possible that such a feature could have been hidden from other experiments, as there are fewer data points available to witness this pattern. A similar trend has been seen in liquid xenon at energies below 10 keVnr [39], indicating that there is some underlying process responsible for these observations.

Quenching factors for silicon recoils in Si, argon in Ar, germanium in Ge and xenon in Xe have been derived from SRIM by [29], and compared with predictions from Lindhard theory and experimental data where available. Their results indicate that the nuclear stopping powers predicted

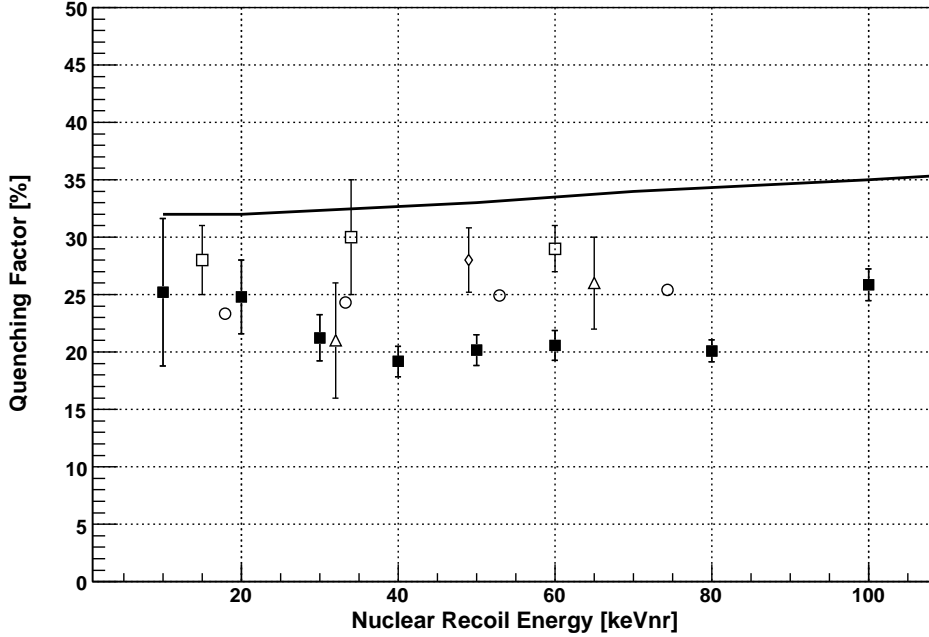


Figure 13. Quenching factor of Na recoils in NaI(Tl). Experimental results from this work (filled black squares), Spooner et al. [17] (open squares), Tovey et al. [18] (open triangles), Gerbier et al. [19] (open circles) and Simon et al. [20] (open diamond) are shown. Additionally, the preliminary theoretical estimation of the quenching factor from Hitachi [25] is represented by the solid black line.

by Lindhard theory and calculated by SRIM differ by 15% at most, although bigger discrepancies are present for the electronic stopping power. When compared with experimental data, the original Lindhard theory is closest to giving an accurate prediction for these media.

Neither Lindhard theory nor the results from SRIM reproduce the shape of the experimental results for Na recoils in NaI(Tl). Unlike the prediction from Hitachi [25], which provides a better resemblance to the pattern seen, they do not consider the effect of electronic quenching due to high LET of ions. However, the appearance of the dip remains unexplained.

6. Conclusion

Quenching factor measurements have been performed for sodium recoils in a 5 cm diameter, cylindrical NaI(Tl) crystal. The results show an average quenching factor of 22.1% at energies less than 50 keVnr, in agreement with other measurements. Results from simulations confirm that the contribution from multiple scattering events provides a featureless background, and can be neglected. The results do not reproduce the shape of the predicted curves from Lindhard theory, and SRIM and TRIM. However, the predicted quenching factor from Hitachi [25], which takes electronic quenching into account, compares favourably with the experimental results. The presence of a dip in the quenching factor at around 40 keVnr is observed.

Scattering angle	Recoil energy	Measured energy	Quenching factor
θ [°]	E_R [keVnr]	E_{vis} [keVee]	Q [%]
18.4	10	2.52 ± 0.90	25.2 ± 6.4
26.1	20	4.96 ± 0.88	24.8 ± 3.2
32.1	30	6.37 ± 0.79	21.2 ± 2.0
37.3	40	7.67 ± 0.69	19.2 ± 1.3
41.9	50	10.08 ± 0.81	20.2 ± 1.3
46.1	60	12.35 ± 0.91	20.6 ± 1.3
53.8	80	16.07 ± 0.88	20.1 ± 1.0
60.7	100	25.86 ± 1.49	25.9 ± 1.4

Table 2. Quenching factors of Na nuclear recoils relative to those of gamma-rays of the same energy. The average scattering angle is given by θ (column 1), the average recoil of the Na nucleus is given by E_R (column 2) and the measured energy is given by E_{vis} (column 3). The fractional contribution from statistical errors remains constant at ≈ 0.05 over the full energy range. The systematic error is dominated by uncertainties in the determination of the scattering angle. A marked increase in the contribution from the systematic error is seen at low θ , where $E_R < 20$ keVnr. At higher recoil energies, a reduction in the relative contribution of the systematic error is seen, as it decreases by just under an order of magnitude over the full energy range. Systematic and statistical errors are added quadratically to obtain the uncertainty on the quenching factor.

Acknowledgments

The authors would like to thank Prof. Akira Hitachi for valuable discussions of the results, and the provision of a preliminary theoretical prediction of the quenching factor. HC would also like to thank STFC (formally PPARC) for the support of a PhD studentship. This work has partly been supported by the ILIAS integrating activity (Contract No. RII3-CT-2004-506222) as part of the EU FP6 programme in Astroparticle Physics.

References

- [1] Y. Sofue & V. Rubin, *Rotation curves of spiral galaxies*, *Ann. Rev. Astron. Astrophys.* **39** (2001) 137 [astro-ph/0010594].
- [2] R. A. Cabanac, D. Valls-Gabaud, A. O. Jaunsen, C. Lidman & H. Jerjen, *Discovery of a high-redshift Einstein ring*, *Astron. Astrophys.* **436** (2005) L21 [astro-ph/0504585].
- [3] D. N. Spergel et al., *Three-year Wilkinson Microwave Anisotropy Probe (WMAP) observations: implications for cosmology*, *Astrophys. J. Suppl.* **170** (2007) 377 [astro-ph/0603449].
- [4] S. Burles, K. M. Nollett & M. S. Turner, *Big bang nucleosynthesis predictions for precision cosmology*, *Astrophys. J.* **552** (2001) L1 [astro-ph/0010171].
- [5] N. J. C. Spooner, *Direct dark matter searches*, *J. Phys. Soc. Jap.* **76** (2007) 111016 [arXiv:0705.3345].
- [6] J. J. Quenby et al., *Results from the first stage of a UK Galactic dark matter search using low background sodium iodide detectors*, *Phys. Lett. B* **351** (1995) 70.

- [7] J. Amaré et al., *Dark matter searches with NaI scintillators in the Canfranc underground laboratory: ANAIS experiment*, *J. Phys. Conf. Ser.* **39** (2006) 123.
- [8] R. Bernabei et al., *Searching for WIMPs by the annual modulation signature*, *Phys. Lett. B* **424** (1998) 195.
- [9] K. Fushimi et al., *Limits on the annual modulation of WIMPs-nucleus scattering with large-volume NaI(Tl) scintillators*, *Astropart. Phys.* **12** (1999) 185.
- [10] R. Bernabei et al., DAMA Collaboration, *Search for WIMP annual modulation signature: results from DAMA/NaI-3 and DAMA/NaI-4 and the global combined analysis*, *Phys. Lett. B* **480** (2000) 23.
- [11] B. Ahmed et al., *The NAIAD experiment for WIMP searches at Boulby mine and recent results*, *Astropart. Phys.* **19** (2003) 691 [hep-ex/0301039].
- [12] G. J. Alner et al., UKDMC, *Limits on WIMP cross-sections from the NAIAD experiment at the Boulby Underground Laboratory*, *Phys. Lett. B* **616** (2005) 17 [hep-ex/0504031].
- [13] R. Bernabei et al., *Highlights of DAMA*, *J. Phys. Conf. Ser.* **39** (2006) 82.
- [14] J. B. Birks, *The theory and practice of scintillation counting*, Pergamon Press, London 1964.
- [15] R. Voltz, J. Lopes da Silva, G. Laustriat & A. Coche, *Influence of the nature of ionizing particles on the specific luminescence of organic scintillators*, *J. Chem. Phys.* **45** (1966) 3306.
- [16] J. D. Lewin & P. F. Smith, *Review of mathematics, numerical factors, and corrections for dark matter experiments based on elastic nuclear recoil*, *Astropart. Phys.* **6** (1996) 87.
- [17] N. J. C. Spooner et al., *The scintillation efficiency of sodium and iodine recoils in a NaI(Tl) detector for dark matter searches*, *Phys. Lett. B* **321** (1994) 156.
- [18] D. R. Tovey et al., *Measurement of scintillation efficiencies and pulse-shapes for nuclear recoils in NaI(Tl) and CaF₂(Eu) at low energies for dark matter experiments*, *Phys. Lett. B* **433** (1998) 150.
- [19] G. Gerbier et al., *Pulse shape discrimination and dark matter search with NaI(Tl) scintillator*, *Astropart. Phys.* **11** (1999) 287.
- [20] E. Simon et al., *SICANE: a detector array for the measurement of nuclear recoil quenching factors using a monoenergetic neutron beam*, *Nucl. Instrum. Meth. A* **507** (2003) 643 [astro-ph/0212491].
- [21] J. Lindhard, M. Scharff & H. E. Schiøtt, *Range concepts and heavy ion ranges (notes on atomic collisions, II)*, *Mat. Fys. Medd. Dan. Vid. Selsk.* **33** (1963) 14.
- [22] J. Lindhard, V. Nielsen, M. Scharff & P. V. Thomsen, *Integral equations governing radiation effects (notes on atomic collisions, III)*, *Mat. Fys. Medd. Dan. Vid. Selsk.* **33** (1963) 10.
- [23] I. S. Tilinin, *Quasiclassical expression for inelastic energy losses in atomic particle collisions below the Bohr velocity*, *Phys. Rev. A* **51** (1995) 3058.
- [24] A. Hitachi, *Properties of liquid xenon scintillation for dark matter searches*, *Astropart. Phys.* **24** (2005) 247.
- [25] A. Hitachi, *Liquid rare gases and inorganic scintillators for WIMP searches*, in *The identification of dark matter: proceedings of the 6th international workshop*, September, 11–16, 2006 Rhodes, Greece, 344.
- [26] D. W. Aitken, B. L. Beron, G. Yenicay & H. R. Zulliger, *The fluorescent response of NaI(Tl), CsI(Tl), CsI(Na) and CaF₂(Eu) to X-rays and low energy gamma rays*, *IEEE Trans. Nucl. Sci.* **14**(1) (1967) 468.

- [27] B. D. Rooney & J. D. Valentine, *Scintillator light yield nonproportionality: calculating photon response using measured electron response*, *IEEE Trans. Nucl. Sci.* **44**(3) (1997) 509.
- [28] J. F. Ziegler, J. P. Biersack & U. Littmark, *SRIM/TRIM version 2006.02*, <http://www.srim.org>.
- [29] A. Mangiarotti et al., *A survey of energy loss calculations for heavy ions between 1 and 100 keV*, *Nucl. Instrum. Meth. A* **580** (2007) 114 [physics/0610286].
- [30] Electron Tubes Ltd., Bury Street, Ruislip, Middlesex HA4 7TA, United Kingdom, <http://www.electrontubes.com>.
- [31] S. Agostinelli et al., GEANT4 Collaboration, *GEANT4 – a simulation toolkit*, *Nucl. Instrum. Meth. A* **506** (2003) 250, <http://geant4.cern.ch>.
- [32] H. H. Barschall & M. H. Kanner, *On the angular distribution of fast neutrons scattered by hydrogen, deuterium and helium*, *Phys. Rev.* **58** (1940) 590.
- [33] Acqiris Europe, 18 Chemin des Auix, 1228 Plan-les-Ouates, Geneva, Switzerland, <http://www.acqiris.com>.
- [34] G. J. Alner et al., *The ZEPLIN II dark matter detector: data acquisition system and data reduction*, *Nucl. Instrum. Meth. A* **587** (2008) 101 [astro-ph/0703362].
- [35] R. Brun & F. Rademakers, *ROOT - An object oriented data analysis framework*, *Nucl. Instrum. Meth. A* **389** (1997) 81, <http://root.cern.ch>.
- [36] S. Marrone et al., n_TOF Collaboration, *Pulse shape analysis of liquid scintillators for neutron studies*, *Nucl. Instrum. Meth. A* **490** (2002) 299.
- [37] J. H. Lee & C. S. Lee, *Response function of NE213 scintillator for 0.5–6 MeV neutrons measured by an improved pulse shape discrimination*, *Nucl. Instrum. Meth. A* **402** (1998) 147.
- [38] S. C. Wu et al., *Near threshold pulse shape discrimination techniques in scintillating CsI(Tl) crystals*, *Nucl. Instrum. Meth. A* **523** (2004) 116 [physics/0307002].
- [39] V. Chepel et al., *Scintillation efficiency of liquid xenon for nuclear recoils with the energy down to 5 keV*, *Astropart. Phys.* **26** (2006) 58 [physics/0512136].